Applied Physics Letters

3D printing-assistant method for magneto-active pulse pump: Experiment, simulation, and deformation theory

Cite as: Appl. Phys. Lett. **117**, 241901 (2020); https://doi.org/10.1063/5.0030055
Submitted: 18 September 2020 . Accepted: 20 November 2020 . Published Online: 17 December 2020

Xufeng Cao, Shouhu Xuan, Tao Hu, and Xinglong Gong

Applied Physics Letters ARTICLE scitation.org/journal/apl

3D printing-assistant method for magneto-active pulse pump: Experiment, simulation, and deformation theory

Cite as: Appl. Phys. Lett. **117**, 241901 (2020); doi: 10.1063/5.0030055
Submitted: 18 September 2020 · Accepted: 20 November 2020 ·
Published Online: 17 December 2020

Xufeng Cao, Shouhu Xuan,[a] Tao Hu, and Xinglong Gong[a]

AFFILIATIONS

CAS Key Laboratory of Mechanical Behavior and Design of Materials, Department of Modern Mechanics, CAS Center for Excellence in Complex System Mechanics, University of Science and Technology of China, Hefei 230027, China

[a]Authors to whom correspondence should be addressed: xuansh@ustc.edu.cn and gongxl@ustc.edu.cn

ABSTRACT

This Letter reports a magneto-active pulse pump (MAPP) consisting of a flexible check valve and a magneto-active pipe developed by using a 3D printing-assistant method. The deformation behavior of the magneto-active pipe is investigated by using the three-dimensional reconstruction, simulation, and theoretical analysis. The larger deformation under a high magnetic field produces higher driving pressure, and thus, the MAPP can be used to transfer liquid. It is found that the MAPP responds to the strength and frequency of the magnetic field simultaneously and the pumping performance can be analyzed by a magneto-fluid-solid coupling simulation. This work provides guidance for the design and manufacture of pulse pumps in future heart pump components.

Inspired by heart valves, lymphatic vessels, and skeletal muscles, the micropumps, which can help blood circulation by contraction, received increasing interest in the fluid control field.[1] Among these actuated pumps,[2–4] the magnetic driving pump possesses many advantages such as compact structure, great actuation control, remote non-contact control, and fast response capability.[5–7] During the past decade, most of the effort has been focused on the traditional electromagnetic peristaltic pumps,[8–11] while the pulse pump is rarely mentioned. A certain range of static and alternating magnetic fields have been proven to be safe in magnetic resonance imaging and magnetic hyperthermia.[12–15] Therefore, owing to the unique pulse pumping performance, the designation of the magneto-active pulse pump (MAPP) becomes attractive in the biomedical field as the blood pump or heart pump components. High flexibility, great mechanical property, and good fatigue endurance are highly required for the actuating pipe in the electromagnetic pump system. Because of the easy deformation and rapid response to the magnetic field, magnetic polymers have attracted extensive attention as actuating pipes, which greatly promoted the development of electromagnetic pumps.[11,16,17] The deformation behavior of the soft magneto-active pipe is of great significance since it plays a key role in the pumping capacity. Upon the external magnetic field, the generated magnetic force induces the deformation of the soft magneto-active materials. Although a series of studies have been conducted on magnetic field-induced deformation,[18–22] the detailed mechanism is still mysterious. The previous reports indicated that the deformation of the magnetorheological elastomers showed a high response to the magnetic field due to the strong magnetic carbonyl iron (CI) particles in the composite.[23] As a result, developing a high-performance magneto-active composite-based MAPP and investigating its pulse deformation mechanism are urgently required.

In this study, we revealed the deformation mechanism and explored the liquid-pumping capability of MAPP based on the magnetorheological elastomer. The MAPP consisting of a flexible check valve and a magneto-active pipe was developed by a 3D printing-assistant method. A three-dimensional scanning system (OKIO ColorScan-400, Beijing Tianyuan 3D Technology Co., Ltd., China) was used to measure the collapse deformation of magneto-active pipe. The finite element method (COMSOL Multiphysics 5.4) was adopted to simulate the deformation characteristics of magneto-active pipe and the flow behavior of MAPP. This work possesses high potential for guiding the design and manufacture of a smart pulse pump.

Figure 1(a) shows the fabrication processes of MAPP, in which the ABS pipe mold was developed by the fused deposition modeling 3D printing method and then the magneto-active pipe was formed by injecting the magnetorheological elastomers precursor into the mold. The check valve was directly fabricated by 3D jetting technology. After

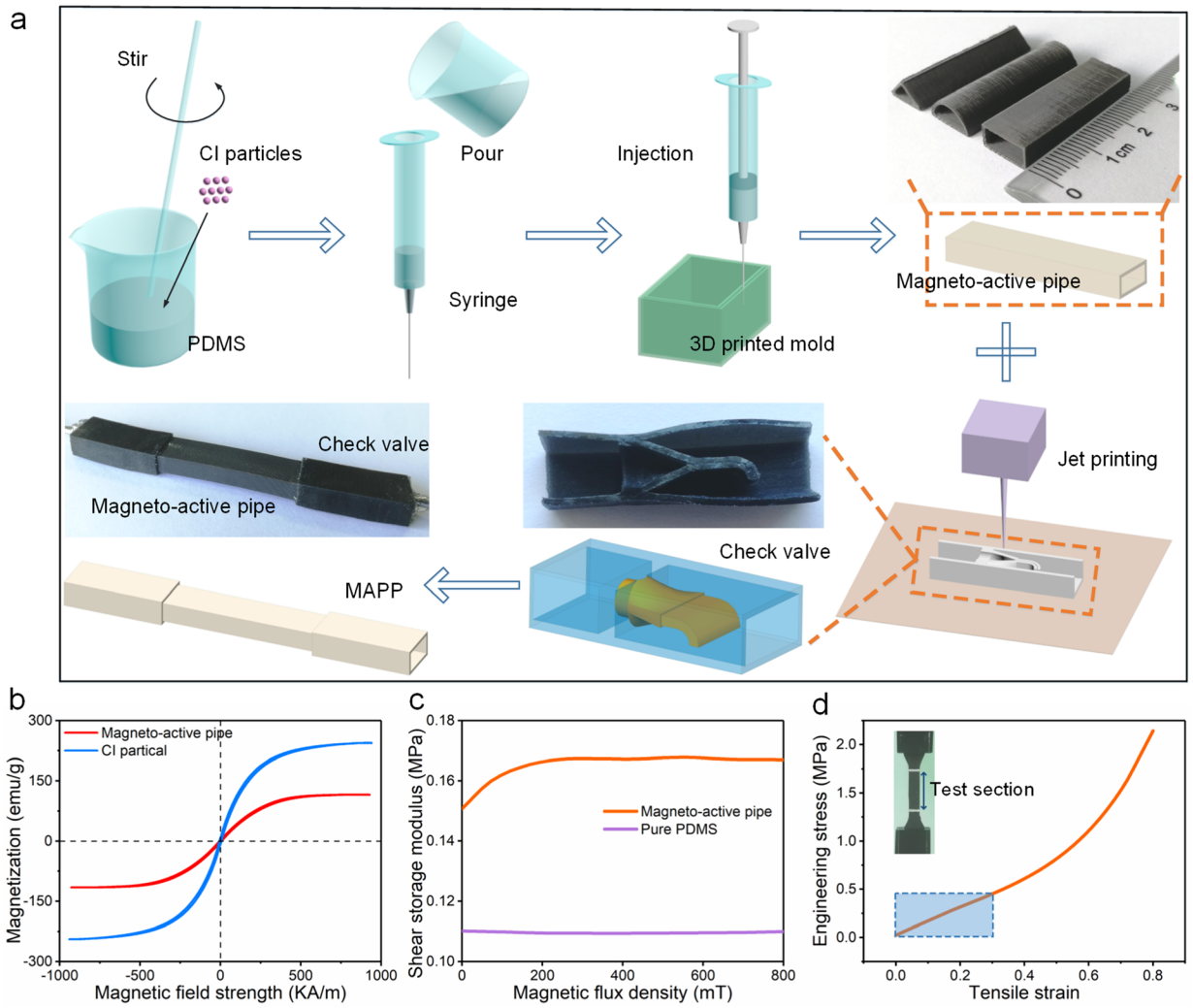

FIG. 1. (a) Fabrication processes of MAPP. (b) Vibrating sample magnetometer data. (c) The storage modulus vs the magnetic flux density curves. (d) Tensile stress-strain curve.

connecting the check valve to both ends of the magneto-active pipe, the MAPP was obtained and the detailed fabrication procedure is described in Sec. I of the supplementary material. Due to the easy 3D printing-assistant method, the magneto-active pipe with different cross section shapes (trilateral, semicircle, and rectangle) could be facilely constructed. First, the detailed magnetic and mechanic properties of the magnetorheological elastomers were investigated. The hysteresis loop [Fig. 1(b)] showed that the residual magnetization and coercivity were almost zero, which allowed magnetorheological elastomers with easy changes in the magnetic properties. Meanwhile, the storage modulus increased with the magnetic field and reached equilibrium when the magnetic flux density exceeded 300 mT, indicating a typical magnetorheological behavior [Fig. 1(c)]. Moreover, the tensile stress-strain curve of material was obtained by using digital images for calibration to reduce the inaccuracy of results by using the dumbbell shaped samples.[24] The tensile stress-strain curve of the magnetorheological elastomers demonstrated that this material had an excellent elastic deformation behavior below the 30% strain [Fig. 1(d)]. In summary, the magneto-active pipe showed a good magnetic response capability and an ideal elasticity under small deformation.

The influence of the magnetic field on the deformation of magneto-active pipe was investigated by a three-dimensional reconstruction. For details regarding the experimental design, simulation of the magnetic field distribution, and choice about the cross section of pipe, refer to Sec. II in the supplementary material. The magnetic force-dependent deformation of the pipe was directly related to the magnitude and gradient of the magnetic field. The field strength and gradient increased with the number of magnets [Figs. S1(d) and S1(e)]. For convenience, the magnitude of the magnetic field (one-to-one correspondence between magnitude and the gradient) was used in the following discussion. As seen in Figs. 2(e)–2(g), upon increasing the magnetic field from 75 to 145 and 175 mT, the deformation increased significantly in coinciding with the collapse deformation of the pipe. Figure 2(h) shows $\Delta V/V$ increasing from 2.2% to 62.3%

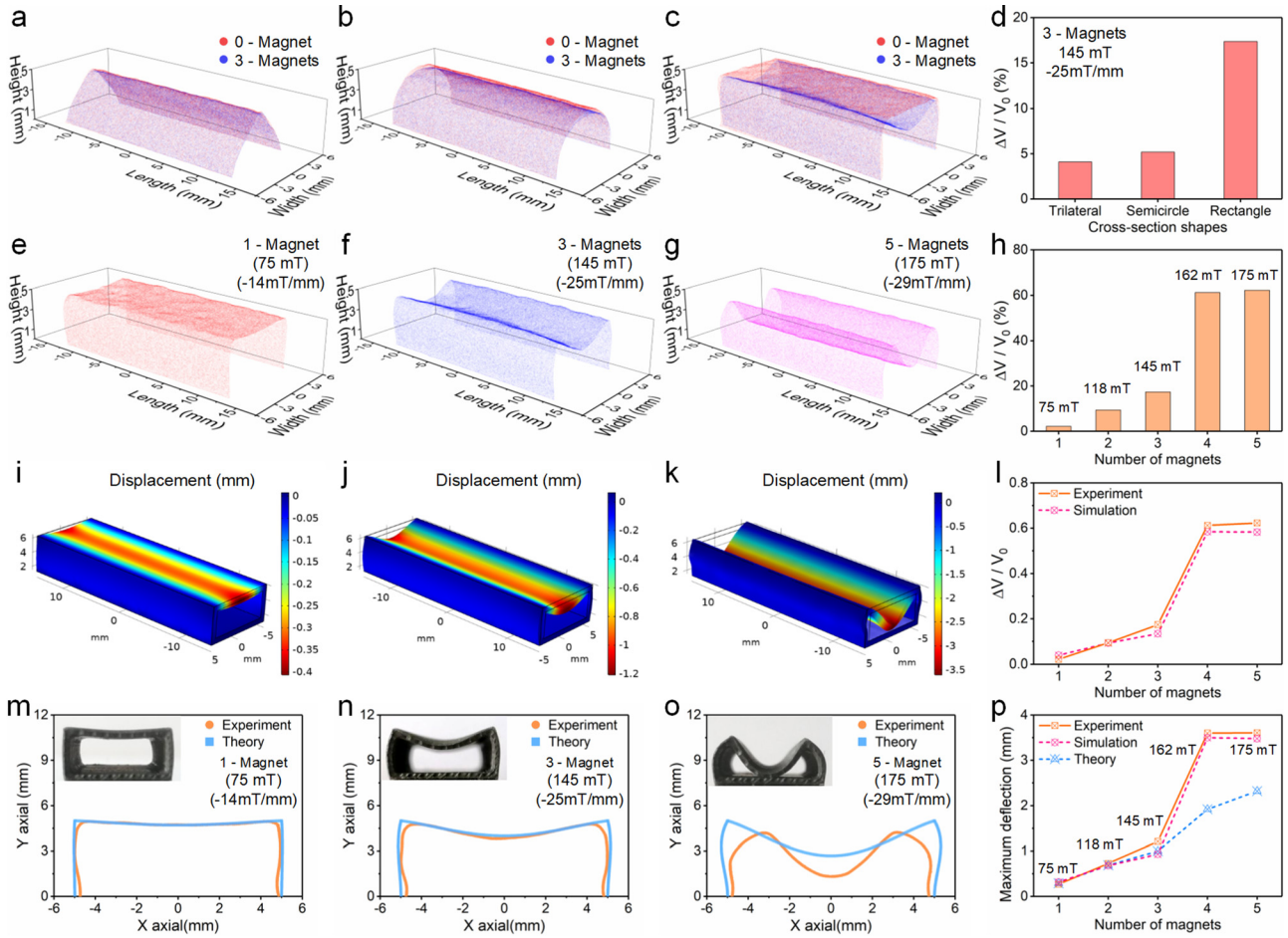

FIG. 2. Deformation analysis. (a)–(c) Three-dimensional shape of pipe with different cross-sectional shapes. (d) The volume change rate of pipe with different cross-sectional shapes. (e)–(g) Three-dimensional shape of pipe under different magnetic fields. (h) The experiment volume change rate of rectangle pipe under different magnetic fields. (i)–(k) The deformation simulation corresponding to experiment in Figs. 2(e)–2(g). (l) Experiment and simulation value of the volume change rate. (m)–(o) Experimental and theoretical deflection curves. (p) The experimental, simulated, and theoretical value of the maximum deflection.

with the magnetic field increasing from 75 to 175 mT. Obviously, when the magnetic field changed from 145 to 162 mT, the volume change rate ($\Delta V/V$) had a sharp increase from 17.4% to 61.3%. Then, upon further increasing the magnetic field, $\Delta V/V$ remained unchanged. These results showed that the pipe structure became unstable when the magnetic force was large enough, and the bending deformation continuously increased until the upper wall came into contact with the lower wall.

Furthermore, to optimize the magnetic field-dependent response of the magneto-active pipe, the deformation under different magnetic fields was simulated by a finite element method (COMSOL Multiphysics 5.4). Figures 2(i)–2(k) show the representative deformation simulation result that corresponded to the experimental result in Figs. 2(e)–2(g). Obviously, due to the geometric symmetry of the pipe and magnet, the deformation was also axially symmetric. So the maximum deflection of the upper wall was in the central axis position. The simulations confirmed and quantified the intuitive notion that the deformation increased with the magnetic field. In addition, the volume change rate was also calculated. The simulated results of $\Delta V/V$ basically coincided with the experimental value, which indicated the validity of the simulation model [Fig. 2(l)]. More importantly, the simulation could not only quantitatively describe the deformation but also guide the design and deformation prediction of different magneto-active pipes.

Herein, the deformation of the magneto-active pipe was also theoretically analyzed to better understand the deformation principle. As shown in Fig. S1(f), the bending deformation of the magneto-active pipe could be simplified as the deflection of a steel frame fixed at both ends. The load was the magnetic force between the pipe and the magnet. Herein, the rectangular cross section was selected for further analysis. The magnetic field distribution along the Z direction of the magnet could be expressed as[25]

$$\begin{aligned} B_z = -K(&f[y, a-x, z] + f[b-y, a-x, z] + f[x, b-y, z] \\ &+ f[a-x, b-y, z] + f[b-y, x, z] + f[y, x, z] \\ &+ f[a-x, y, z] + f[x, y, z]), \end{aligned} \tag{1}$$

where $f[\mathrm{x1},\mathrm{x2},\mathrm{x3}] = \mathrm{ArcTan}\left[\frac{\mathrm{x1}}{\mathrm{x2}}\frac{\mathrm{x3}-c}{\sqrt{\mathrm{x1}^2+\mathrm{x2}^2+(\mathrm{x3}-c)^2}}\right] - \mathrm{ArcTan}\left[\frac{\mathrm{x1}}{\mathrm{x2}}\frac{\mathrm{x3}}{\sqrt{\mathrm{x1}^2+\mathrm{x2}^2+\mathrm{x3}^2}}\right]$ and a, b, and c are the length, width, and height of the magnet, respectively. K is a coefficient that could be obtained by experimentally measuring the magnetic field. The gradient of magnetic field distribution along the Z direction could be calculated by taking the partial derivative of Bz,

$$\mathrm{d}B_z = \partial_z B_z. \tag{2}$$

When the magnets were arranged in the Z direction (magnetizing direction), Bz and $\mathrm{d}Bz$ could be superimposed vectorially. For magnetic materials placed in an external magnetic field, the magnetization M and the magnetic field H had the following relationship: $M = \chi_m H$, where χ_m is the magnetic susceptibility of materials. The magnetic flux density B was defined as $B = \mu_0(H + M)$, where μ_0 is the permeability of vacuum. Thus, the magnetization of the magnetic polymer was

$$M = (u_r - 1)H = \frac{(u_r - 1)}{u_0 u_r}B, \tag{3}$$

where u_r is the relative permeability calculated by $u_r = 1 + \frac{3\text{ø}(4+\text{ø})}{4(1-\text{ø})}$[26] and ø is the volume fraction of CI particles. The gravity was ignored due to the light and thin structure, and so only the magnetic force between pipe and the magnet was taken into consideration, which was given as $f_m = M \cdot \nabla B$.[27] In order to simplify the calculation, the force on the sidewall was ignored and the force on the upper wall was simplified to a uniform load along the width direction due to a smaller change in the magnetic field. Combining the equations mentioned above, the uniform load q could be calculated as

$$q = f_m l\delta = \frac{l\delta(u_r - 1)}{u_0 u_r}B_z \mathrm{d}B_z, \tag{4}$$

where l and δ are the length and thickness of pipe, respectively. Herein, the deformation of the symmetry plane was selected to show the deformation of all the cross section. Thus, the deflection curve equation of the structure was obtained by integrating the bending moment equation,

$$w(X)_{\text{upper wall}} = \frac{2}{E\delta^2}\left(\frac{X^4}{4} - \frac{mX^3}{2} + \frac{m^2X^2}{5} + \frac{m^3X}{20}\right)\frac{(u_r - 1)}{u_0 u_r}B_z \mathrm{d}B_z \tag{5}$$

and

$$w(Y)_{\text{sidewall}} = \frac{4(n^2Y^2 - nY^3)}{5E\delta^2}\frac{(u_r - 1)}{u_0 u_r}B_z \mathrm{d}B_z, \tag{6}$$

where m and n are the width and height of pipe and E is Young's modulus. In addition, the volume change was also obtained by $\Delta V = l\left[\int_0^m |w(X)|dX - 2\int_0^n |w(Y)|dY\right]$.

Figures 2(m)–2(o) exhibit the representative experimental and theoretical deflection curves in the equilibrium state under the magnetic field of 75, 145, and 175 mT, respectively. The results showed that the deflection curves were symmetrical and the maximum deformation occurred at the center of the upper wall. Moreover, the theoretical and experimental deflection curves coincided with each other. The experimental maximum deflection increased from 0.27 to 3.6 mm upon increasing the magnetic field from 75 to 175 mT [Fig. 2(p)]. As expected, the bending deformation increased with the magnetic field. Consistent with the previous deformation measurement, the structure instability resulted in the sharp increase of deflection from 1.21 to 3.6 mm when the magnetic force reached the critical load. Then, the deflection remained unchanged as the magnetic field further increased. The deflection simulation and the experimental results were in good agreement. However, due to the limitation of the theoretical model, the deformation after buckling instability could not be obtained by analytical solutions. Because once buckling instability occurs, the structure could not continue to bear the load, and the deformation increased sharply. In the experiment, because the lower wall of the pipe prevented the further increment of the deformation, the deflection of the buckling instability in this state was measured. In order to reduce the error and qualitatively estimate the deflection after instability, the magnetic field and gradient magnetic field at the calculated deflection position would be substituted into formula (4) again to calculate the final deflection. In summary, the simplified model could quantitatively explain the deformation before instability and was beneficial to predict the deformation properties of the magneto-active pipe with different geometric parameters.

The magneto-active pipe can be applied in constructing the MAPP by connecting the check valve to both ends of pipe. An electromagnet was used to generate the magnetic field for improving the actuation efficiency and controllability of the MAPP. The cyclic magnetic test was first carried out, which had guidance for applying the magnetic field in the subsequent pumping experiments (Secs. III and IV in the supplementary material). Figure 3(a), Multimedia view, shows the digital image and schematic diagram of the MAPP system. The breakthrough and backflow pressures of the 3D printed check valve are shown in Fig. 3(b). The magneto-active pipe was deformed and collapsed by the magnetic force. Similar to a beating heart driving blood, the magneto-active pipe generated a driving pressure that opened the outlet valve and closed the inlet one, pumping the liquid in it through the check valve. After applying and removing the magnetic field continuously, the liquid in the inlet was quickly transferred to the outlet. The influence of the loading period and the magnetic field on pumping efficiency was studied. Obviously, the larger the magnetic field, the higher the flow rate of MAPP [Fig. 3(c)]. When the magnetic fields were changed from 175 to 200 mT, the flow rate increased sharply. It was found that when the magnetic force exceeded the critical load, the structure became unstable, resulting in a sharp change in the deformation and flow rate. Moreover, when the magnetic fields were kept at 150 and 175 mT, the flow rate decreased from 4.6 and 7.2 to 2.2 and 3.6 μl/s as the frequency increases from 0.2 to 1 Hz, respectively [Figs. 3(d)–3(e)]. Due to the slow deformation of the flexible check valve, partial backflow was generated, which offsets most of the pumping volume. The opening time of the check valve increased with the loading frequency and further decreased with the pumping flow rate. When the magnetic fields were 200 and 225 mT, the pumping rate increased significantly from 21.3 and 25.8 to 29.9 and 32.9 μL/s with the increasing frequency, respectively [Figs. 3(f)–3(g)]. This was because the ratio of the backflow volume to the pumping volume became small, and the loading frequency played a major role at this time. Therefore, the flow rate was mainly dependent on the magnitude of the magnetic field and was partly affected by the loading period.

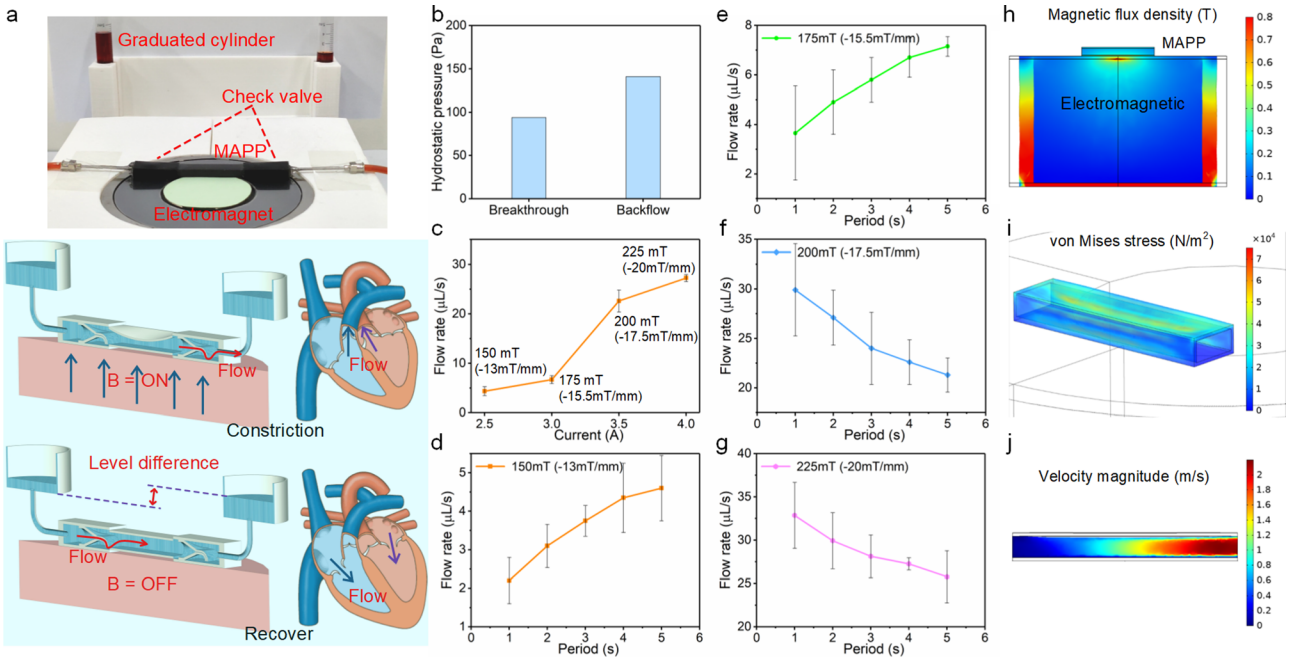

FIG. 3. (a) The digital image and schematic diagram of the MAPP system. (b) The breakthrough and backflow pressure of the 3D printed check value. (c) Plot of flow rate vs current. (d)–(g) Plots of flow rate vs period under different magnetic fields. (h) The detailed magnetic field distribution. (i) The Mises stress distribution. (j) The fluid velocity in the flow direction of the cross section. Multimedia view: https://doi.org/10.1063/5.0030055.1

Furthermore, a finite element model was established to simulate the magnetic field distribution, Mises stress distribution, and fluid velocity in the steady state under the current of 3 A (Sec. IV in the supplementary material). Figure 3(h) illustrates that the magnetic field distribution inside the magneto-active pipe was between 203 and 432 mT. The Mises stress distribution of the pipe showed that the maximum stress occurred at the maximum deflection of the upper wall and on the edge of pipe [Fig. 3(i)]. The fluid velocity in the flow direction of the cross section is shown in Fig. 3(j). As expected, the velocity near the outlet was maximum. This effective simulation model provided the influence of the magnetic field on the pump performance, thereby further guiding the design of the pulse pump. In summary, the MAPP had easy response capability, good actuation controllability, and high pump efficiency, as well as good stability when the pump was stopped working.

In summary, this work reported a MAPP consisting of a flexible check valve and magneto-active pipe. The deformation behavior and pump performance of the MAPP were studied via experiment, simulation, and theory analysis. With the increasing magnetic field, the collapse deformation of pipe increased significantly. It generated higher driving pressure to pump the liquid through the check valve. The flow rate achieved was 32.9 μl/s under a magnetic field of 225 mT at the frequency of 1 Hz. As a result, the MAPP was demonstrated to have simple response capability, good actuation controllability, and high pump efficiency. This work facilitated the development of smart pulse pumps and their potential application in microfluidics, heart pump components, etc.

See the supplementary material for additional experimental details, deformation characteristic analysis, magnetic field distribution, response time data, and video of the magneto-active pulse pump.

Financial support from the National Natural Science Foundation of China (Grant Nos. 11822209, 11972343, and 12072338), the Joint Fund of USTC-National Synchrotron Radiation Laboratory (No. KY2090000055), the Fundamental Research Funds for the Central Universities (WK2480000007), and the Strategic Priority Research Program of the Chinese Academy of Sciences (Grant No. XDB22040502) is gratefully acknowledged.

DATA AVAILABILITY

The data that support the findings of this study are available within this article and its supplementary material. Raw data of this study are available from the corresponding author upon reasonable request.

REFERENCES

[1]S. Mohith, P. N. Karanth, and S. M. Kulkarni, Mechatronics **60**, 34 (2019).
[2]Z. Li, J. Zhu, C. C. Foo, and C. H. Yap, Appl. Phys. Lett. **111**, 212901 (2017).
[3]H. Y. Tan, W. K. Loke, and N.-T. Nguyen, Sens. Actuators, B **151**, 133 (2010).
[4]K. Khoshmanesh, S.-Y. Tang, J. Y. Zhu, S. Schaefer, A. Mitchell, K. Kalantar-Zadeh, and M. D. Dickey, Lab Chip **17**, 974 (2017).
[5]S. H. Kim, C. H. Yu, and K. Ishiyama, J. Appl. Phys. **117**, 17B311 (2015).
[6]J. F. Liu, S. Yadavali, A. Tsourkas, and D. Issadore, Lab Chip **17**, 3796 (2017).
[7]B. Kavcic, D. Babic, N. Osterman, B. Podobnik, and I. Poberaj, Appl. Phys. Lett. **95**, 023504 (2009).
[8]R. Fuhrer, C. M. Schumacher, M. Zeltner, and W. J. Stark, Adv. Funct. Mater. **23**, 3845 (2013).

[9]M. M. Said, J. Yunas, B. Bais, A. A. Hamzah, and B. Y. Majlis, Micromachines **9**, 13 (2017).
[10]M. Tahmasebipour and A. A. Paknahad, J. Micromech. Microeng. **29**, 075014 (2019).
[11]S. Y. Tang, X. Zhang, S. Sun, D. Yuan, Q. Zhao, S. Yan, L. Deng, G. Yun, J. Zhang, S. Zhang, and W. Li, Adv. Funct. Mater. **28**, 1705484 (2018).
[12]S. Sammet, Abdom. Radiol. **41**, 444 (2016).
[13]A. Boutet, I. Hancu, U. Saha, A. Crawley, D. S. Xu, M. Ranjan, E. Hlasny, R. Chen, W. Foltz, F. Sammartino, A. Coblentz, W. Kucharczyk, and A. M. Lozano, J. Neurosurg. **132**, 586 (2020).
[14]J. Carrey, V. Connord, and M. Respaud, Appl. Phys. Lett. **102**, 232404 (2013).
[15]D. Chang, M. Lim, J. A. C. M. Goos, R. Qiao, Y. Y. Ng, F. M. Mansfeld, M. Jackson, T. P. Davis, and M. Kavallaris, Front. Pharmacol. **9**, 831 (2018).
[16]B. L. Gray, J. Electrochem. Soc. **161**, B3173 (2014).
[17]T. Nakahara, Y. Ueda, H. Miyagawa, H. Kotera, and T. Suzuki, J. Micromech. Microeng. **30**, 025006 (2020).
[18]A. Hamann and E. D. Dahlberg, Appl. Phys. Lett. **110**, 091906 (2017).
[19]R. M. Erb, J. J. Martin, R. Soheilian, C. Pan, and J. R. Barber, Adv. Funct. Mater. **26**, 3859 (2016).
[20]S. Qi, H. Y. Guo, J. Fu, Y. P. Xie, M. Zhu, and M. Yu, Compos. Sci. Technol. **188**, 107973 (2020).
[21]X. Hou, Y. Liu, G. Wan, Z. Xu, C. Wen, H. Yu, J. X. J. Zhang, J. Li, and Z. Chen, Appl. Phys. Lett. **113**, 221902 (2018).
[22]Y. Kim, H. Yuk, R. Zhao, S. A. Chester, and X. Zhao, Nature **558**, 274 (2018).
[23]W. Gao, L. Wang, X. Wang, and H. Liu, ACS Appl. Mater. Interfaces **8**, 14182 (2016).
[24]I. D. Johnston, D. K. McCluskey, C. K. L. Tan, and M. C. Tracey, J. Micromech. Microeng. **24**, 035017 (2014).
[25]X. F. Guo, Y. Yang, and X. J. Zheng, Appl. Math. Mech. **25**, 297 (2004).
[26]H. M. Yin and L. Z. Sun, Phys. Rev. B **72**, 054409 (2005).
[27]T. H. Boyer, Am. J. Phys. **56**, 688 (1988).